Coupled thrust and vorticity dynamics during VRS*

Ömer Savaş
Department of Mechanical Engineering
University of California Berkeley, Berkeley, California, 94720-1740
savas@me.berkeley.edu

Richard B. Green
Department of Aerospace Engineering
University of Glasgow, Glasgow, Great Britain
richardg@aero.gla.ac.uk
and
Francis X. Caradonna
Army RDECOM, Aeroflightdynamics Directorate
NASA Ames Research Center, Moffett Field, California, 94035-1000
caradonna@merlin.arc.nasa.gov

Abstract

The focus is on the vortex ring state (VRS) observed at rapid descent rates. At VRS, the helical vortex filaments coming off the blades amalgamate around the rotor disk forming a vortex ring, which periodically detaches into the wake, causing extreme oscillations in thrust, with periods on the order of several tens of rotor revolutions. We discuss here the phase relation between the thrust cycle and vorticity distribution at the rotor disk. Maxima of the VRS thrust oscillations correlate well with the maxima of circulation, enstrophy, and minima of enstrophy dispersion radius observed in the vicinity of the rotor disk

Introduction

Under certain conditions of descent, typically when the ratio of the descent speed V_z to the hover-induced velocity V_h is around unity, the vortices that usually trail below a rotor disk to form the helical vortex wake collapse into a ring-like structure around the plane of the disk. This is known as the vortex ring state (VRS), and the formation and subsequent breakdown of the ring-like vortex is accompanied by large thrust excursions. In axial descent the thrust excursions are aperiodic, while in non-axial descent a distinct periodicity is observed.

A useful review of the VRS was presented by [Johnson, 2004], and results of some experimental investigations of the VRS were compiled. Experiments were performed as early as the 1920s, for example [Glauert, 1926] and [Lock et al., 1925]. Flow experiments of the VRS were performed as early as 1951, when [Drees and Hendal, 1951] performed a smoke flow visualization of a model helicopter in simulated descent. This experiment served to highlight the large scale and complexity of the VRS flow field. [Stewart, 1951] reported results of in-flight experiments. Later investigations by [Washizu et al., 1966] and [Yaggy and Mort, 1963] investigated the performance aspects of the VRS, and by this time it was widely recognized that the VRS tended to occur when the descent speed was around the same magnitude as the hover induced velocity, and that the onset of the VRS was accompanied by thrust oscillations and a requirement for more power. Some more recent experiments to investigate performance in VRS have revealed that in descent at low forward speed the thrust oscillations are greater than in axial descent and have a period of many rotor revolutions ([Betzina, 2001], and also [Stack et al., 2005]). In the latter investigation, flow visualization experiments were also performed which allowed the wake state to be correlated with the phase of the thrust oscillation; the thrust was observed to be a minimum when the vortex ring was just above the plane of the disk, and the thrust would recover to the max-

*Presented at the AHS Specialist's Conference on Aeromechanics, San Francisco, CA, Jan. 23-25, 2008.

imum value as the vortex ring broke down. Other flow visualization experiments have been reported by, among others, [Brinson and Ellenrieder, 1998], who reported a region of reverse flow below the rotor disk in VRS, and [Leishman, 2000], who used a shadowgraph technique to show an accumulation of vortex filaments around the rotor blade tip. From a theoretical standpoint the use of extensively modified actuator disk theory and streamtube models has received much attention (for example [Spalart, 2003]), and [Cuerva et al., 2006] used a combined blade element and momentum theory to predict time-averaged thrust and torque. Elsewhere numerical modeling of the VRS (free wake modeling by [Bhagwat and Leishman, 2000], detailed computational fluid dynamics by [Brown et al., 2004]) has highlighted the importance of the modeling approach to the vortex wake, and simulations of the VRS over very large non-dimensional times are now possible. Linear stability analysis has proved to be useful ([Bhagwat and Leishman, 2000], where the wake was shown to be unstable), but only a fully nonlinear stability theory can explain the gross change of wake topology from a helicoidal shape to a toroidal one. In spite of these advances in numerical predictions of VRS wake flows, there have been relatively few studies of the wake flow using contemporary measurement methods. This is very probably a result of the demanding nature of the application, where the range of flow scales is large and the flow is highly unsteady but evolves over very long periods of time. Without such experimental studies there will be little information for validation of CFD codes or to guide theoretical analysis. Quantitative measurements of large areas of the vortex wake using particle image velocimetry (PIV) have been performed by [Newman et al., 2003], where it was seen that the flow was highly unsteady, and by [Green et al., 2005], where the flow-field unsteadiness in axial descent was seen to take the form of distinct fluid dynamic modes.

The current study extends those by [Stack et al., 2005] and [Green et al., 2007]. Simultaneous thrust and PIV measurements are used to explore the relations between the VRS thrust oscillation and vorticity distributions.

Experimental method

A three-bladed rotor of radius $R = 12.7cm$ was employed in these experiments (figure 1). The blade pitch angles are set manually. The blades , which were 9.5 cm long, were molded from carbon fiber reinforced plastic. The blades were untapered, with a 1.9 cm chord, and had a twist of about 5°. The low blade twist was chosen in order to minimize flow separation at the inherently low Reynolds numbers of the experiments. The blade airfoils were modified ARAD-10 at the tip and modified ARAD-13 at the root. The airfoil modifications included a chordwise-linear thickness increase which thickened the trailing edge and provided more room for the dye/air tubes. In addition, the aft camber of the root airfoil was increased. The experiments were performed in the $67m$ long $\times$ $2.4m$ wide $\times$ $1.65m$ deep towing tank at the University of California, Berkeley. A schematic diagram of the apparatus (top view of the carriage) is shown in figure 2, where an xz-coordinate system is also defined. The angle between the rotor axis and the towing velocity U was varied to simulate different descent angles α ($\alpha = 90^\circ$ being axial descent). Hence, the descent speed was $V_z = Usin\alpha$. Rotor thrust T was measured by strain gauges mounted on flexures. The rotational speed n of the rotor and collective angle θ of the blades could be varied. At $n = 4Hz$ and $\theta = 11.6^o$ the hover thrust coefficient $C_T = T/\rho A V_{tip}^2$ (where A is the rotor disk area and V_{tip} is the rotor blade tip velocity), was $C_T = 0.011$. Illumination was provided by a New Wave Gemini Nd:YAG dual-head laser. The laser sheet is generated and delivered to the flow region through a submerged sealed optical head which consists of a 45° mirror, a positive spherical lens, a negative cylindrical lens and an optical window in contact with water. The head is attached to the end of a vertical periscope tube. Minor adjustments are done by tilting an outside mirror, and lateral sheet positioning by turning the vertical periscope tube. The laser light sheet was aligned with the rotor symmetry plane, and fields of view below and around the rotor disk were viewed. The flow images were recorded using a detachable head Kodak Megaplus ES1.0 camera fitted with Canon lenses. Full rotor view is imaged through a 28mm lens set to $f/1:2$ and blade tip detail views through a 50mm lens set to $f/1:1.4$. The imaged areas of the tip detail views measure about 31cm$\times$31cm (actual settings being 29.9, 30.6, and 31.4 cm-squares). Hence, the approximate image resolution is 0.306 mm/pixel. Image field calibration is done by photographing a square grid at various camera view settings. No noticeable field distortion was observed in the calibration images. The water was seeded with silver-coated, ceramic microspheres with a diameter of $100 \pm 20\mu m$, which had a relative density of $0.9 \pm 0.3\ g/cm^3$. A PIV time delay of $2000\mu s$ was used during the experiments, and the PIV capture rate in terms of velocity fields per second was around 12Hz, which is sufficient for *strobed* time resolution of the development of the VRS. The PIV timing and image acquisition, strain gage data acquisition, towing carriage and rotor systems were all controlled and synchronized with one another through a single C-code running under DOS on a single Windows 2000 PC through appropriate peripheral interfaces. Data for a wide range of descent speeds and angles, fields of view, θ and n were collected. Data analysis of the raw images was performed at high resolution and vorticity ω and other

kinematics have been obtained for the time-resolved data sequences.

Presentation

The flow field statistics for a given run are calculated for the entire field of view, as well as for the individual vortices. Post-processing is done using several codes written in IDL (Interactive Data Language of Research Systems, Inc.). Several integral quantities are used to characterize the whole wake, half-wake, or an individual vortex embedded in the wake. The two-dimensional output fields of our in-house PIV processing code are cropped by 1 step along all four edges to remove the spurious values that exists along the border of the measurement domain. The integration is done over the whole data field when the whole wake or half-wake is imaged and the interest is in the total data field. When describing an individual vortex, the integration is done over the largest circular area that can be centered at the vorticity peak of that vortex without overlapping other vortices in the vicinity. The total circulation $\Gamma(t)$ is obtained from

$$\Gamma(t) = \int \omega dA. \tag{1}$$

The position of the vorticity centroid, $\mathsf{x}_\Gamma = (x_\Gamma, z_\Gamma)$, from

$$\mathsf{x}_\Gamma = \frac{1}{\Gamma}\int \mathsf{x}\,\omega dA \tag{2}$$

where the xz-coordinate system is define in figures 2 and 7. Note that $\mathsf{x}_\Gamma \to \infty$ when $\Gamma \to 0$. To avoid the difficulties in describing the vorticity distribution when vorticity is not all of the same sign, we will appeal to enstrophy ω^2. The total enstrophy $EN(t)$ is determined as

$$EN(t) = \int \omega^2 dA \tag{3}$$

and the position of the enstrophy centroid, $\mathsf{x}_{\mathsf{EN}} = (x_{\mathsf{EN}}, z_{\mathsf{EN}})$, from

$$\mathsf{x}_{\mathsf{EN}} = \frac{1}{EN}\int \mathsf{x}\,\omega^2 dA. \tag{4}$$

As an example, for an equi-strength counter rotating vortex pair, the enstrophy centroid is at the midpoint of the vortices while the vorticity centroid at infinity. A measure of the dispersion of the vorticity field is desired. The dispersion radius of vorticity r_Γ, which is defined as

$$r_\Gamma^2 = \frac{1}{\Gamma}\int |\mathsf{x} - \mathsf{x}_\Gamma|^2 \omega dA \tag{5}$$

may be looked on as an obvious candidate ([Lamb (1938)], [Batchelor (1967)]). This measure works well when vorticity does not change sign over the region of interest. It, however, causes difficulties when vorticity changes sign. The dispersion radius r_Γ can become imaginary for $|\Gamma| < \int |\omega| dA$, and becomes undefined when $\Gamma \to 0$. After [Ortega et al., 2003], to avoid these difficulties, we use an *enstrophy dispersion radius* r_{EN} defined as

$$r_{\mathsf{EN}}^2 = \frac{1}{EN}\int |\mathsf{x} - \mathsf{x}_{\mathsf{EN}}|^2 \omega^2 dA \tag{6}$$

The enstrophy centroid defined in equation 4 gives finite values even when looking at a flow field where $\Gamma \to 0$ and $\mathsf{x}_\Gamma \to \infty$. Parameters based on enstrophy are, however, more susceptible to noise since ω^2 is a second order quantity. Time averaged quantities are denoted as $< >$.

Streamline construction

We will make extensive use of streamline patterns in discussing the flows below. All by themselves, their use is limited. In conjuction with the velocity fields, however, they are rather useful. When discussing comparable flows, we will use streamlines patterns that are drawn from the same set of seed points, to provide some continuity between pictures. One point of caution is due. Even though the measurements are made at the geometric plane of symmetry of the apparatus, they are not measurements at the plane of symmetry of the flow. In fact, the flow does not have any plane of symmetry due to the swirling motion of the helical vortex filaments. There is out-of-plane velocity at the measurement plane. Thus, the streamlines show patterns that reflect this out-of-plane motion. For example, one can observe converging streamlines with decreasing speed which can not happen in the plane of symmetry in an incompressible flow field. The flows are presented from the reference frame of the rotor, hence, we do not expect the streamline patterns to mark the swirling motion associated with individual tip vortices. When the streamline patterns are constructed from the reference frame of a given vortex, then, we do see the swirling signatures of individual vortices.

Results and discussion

Hover and vertical descent

Figure 3 shows PIV results at hover. The rotor speed is 4rev/s, hence, $V_{\mathsf{tip}} = 319$cm/s. The thrust is steady at $C_{\mathsf{T}} = 0.0092$, having only negligible fluctuations (not shown), and hover-induced velocity $V_{\mathsf{h}} = \sqrt{(C_{\mathsf{T}}/2)}\, V_{\mathsf{tip}}$=21.6 cm/s. The PIV camera views the whole vortex wake of the rotor which is

at the top of each of the frames in the figure. The figure shows a sample instantaneous vorticity snapshot $\omega(t_0)$, the average vorticity $<\omega>$ and enstrophy $<\omega^2>$ fields constructed from 150 samples of the full rotor view. The snapshot in figure 3a show the nature of the flow, as well as the actual size of the helical vortex filaments off the tips of the blades. The filament cross sections show variations. Their average shapes in figure 3b and c, are remarkably well defined for the first pitch, due to phase locked PIV sampling employed and the large number of samples used. The helical filaments lose their coherence quickly beyond the first pitch. The line averaged vorticity $\overline{\omega}$ and enstrophy $\overline{\omega^2}$ profiles in the far wake constructed from the lower 3/4 of the frames (marked by vertical bars) are overlaid in their respective frames in the figure. The mean vorticity field in the far field consists of nearly uniform strips of vorticity of alternating sign. The enstrophy profile exhibits a crater profile whose well defined peaks may be taken as markers of the helical wake. The far field diameter of wake defined by the enstrophy peaks in figure 3c is about $1.35R$.

From figure 3a, the filament circulation is estimated as $\Gamma_f = 140\ cm^2/s$, hence the filament Reynolds number of $Re_f = \Gamma_f/\nu = 14,000$. The chord Reynolds number at the blade tip is $Re_c = cV_{tip}/\nu$=60,000 at 4 revs/s. This hover case establishes the baseline for our experiments.

Figure 4 shows average streamline patterns of the rotor in hover, at slow vertical descent and in VRS at rapid vertical descent. The magnitude of the planar velocity field is shown as the background field, essentially presenting the velocity field. The rotor speed is 4 rev/s for all three flows in the figure.

The average streamline pattern for the case of hover is shown in figure 4a and slow descent at V_z=10cm/s (V_z/V_h=0.47) in figure 4b. The thrust coefficient for both cases is about $C_T = 0.009$. The flow patterns look quite similar. The peaks in the velocity magnitude field in the immediate wake of the rotor disk interleave with the peaks in their respective enstrophy fields (cf. figure 4a vs. 3b, c).

The VRS case in rapid descent is shown in (c). The descent speed is 25 cm/s (V_z/V_h=1.16) and the thrust coefficient C_T=0.009. The rotor plane is clearly in the ring vortex formed by the amalgamation of the helical filaments off the blade tips. In fact, in PIV animations, individual filaments are discernible. The average flow pattern is symmetric and corresponding thrust history shows little or no significant oscillations.

Steep oblique descent

Figures 5 and 6 show close-up flow measurements at the leading and trailing edges, respectively, of the rotor disk at rapid descent. The VRS flow shown in the figures is at a descent angle of $\alpha = 60^o$ for $V_z/V_h = 1.0$, $n = 4\ Hz$ and $C_T = 0.011$.

The flow details are shown in figure 5 for the leading edge and in figure 6 for the trailing edge. The traces for thrust $C_T(t)$, circulation $\Gamma(t)$, and enstrophy $EN(t)$ are normalized with their respective maxima. The integration is done over a cropped area that includes the blades, but excludes the rotor hub. In both figures, frames (b) and (c) show the mean vorticity $<\omega>$ and enstrophy $<\omega^2>$ fields, calculated over the duration of each test run. Frames (d) show the instantaneous vorticity field at the maximum thrust and (e) at the minimum thrust of the first VRS oscillation cycle in each figure.

The large scale features of the flow are highly unsteady on both sides of the disk and are on the scale of the rotor disk. On the leading edge side, the vortex zone above the disk expands and contracts; vorticity recirculates and is occasionally shed: this correlates with distinct phases on the thrust cycle, but the flow topology remains essentially unchanged throughout. For the trailing edge, however, there are complete topological changes to the flow as the thrust changes; in the high thrust condition vorticity trails below the rotor, and in the low thrust condition it accumulates around the blade tip and reverse flow penetrates right up to the rotor disk. The mean vorticity and enstrophy fields at the leading are compact (figure 5b, c) while those at the trailing edge are spread widely (figure 6b, c).

The oscillations in this case have a period of about 40 rotor revolutions and the flow topologies observed during the cycle are reminiscent of those observed by [Green et al., 2005] during axial descent. For the leading edge the circulation $\Gamma(t)$ remains positive throughout the cycle and the variation is actually quite small, on the order of 20%; the maximum thrust slightly lags $\Gamma(t)$. On the other hand, the trailing edge flow shows a far more straightforward relationship, with high $C_T(t)$ coinciding with low total $\Gamma(t)$ (negative), and low $C_T(t)$ coinciding with a high value of total $\Gamma(t)$. Enstrophy $EN(t)$, however, is a much more vigorous indicator of the extreme of the thrust. At leading edge, large excursion in $EN(t)$ is observed at the troughs of the thrust history. At the trailing edge, on the other hand, $EN(t)$ exhibits very sharp peaks that accurately mark the maxima of $C_T(t)$. The vorticity fields corresponding to the extrema of $C_T(t)$ at the leading edge are compact (figure 5d, e), being somewhat larger at the troughs . The field there contains patches of positive and negative vorticity during the whole thrust cycle. The vorticity distribution at the trailing edge are quite wide spread and exhibit wide variations during the cycle (figure 6d, e). In particular, the view in figure 6e is fully covered with nearly equal amounts of unmixed positive and negative vorticity, hence the high

value of the $EN(t)$ at the $C_T(t)$ maxima.

Composite Flow Picture

Independent measurements done at the leading and trailing edges of the rotor under the same flow conditions are combined at matched thrust cycle phases to attempt a unified description of the VRS at steep descent. The results are shown in figures 7, 8, and 9. In this reconstruction, flow fields are cropped along the rotor axis and aligned at the rotor disc. The rotor body is masked in the presentation here.

Figure 7a shows the mean flow field averaged over three thrust cycles and averaged over one thrust cycle in figure 7b . Uninterrupted streamlines at the seam along the rotor centerline indicates an acceptable reconstruction. The main features of the flow are that the vorticity is concentrated at the leading edge over the rotor and diffuse at the tailing edge and below the rotor. The streamline pattern at the leading edge is compact and at the tailing edge spread apart and nearly open. Little observable difference exists between the one- and three-cycle averages, indicating a rather repeatable flow behavior.

Figure 8 shows the salient phases of the flow indicated on the thrust cycle. At each point marked on the cycle, about 10 PIV images are averaged to construct the flow pictures in frames a-d in the figure. The flows at the leading edge are qualitatively similar to the cycle averages shown in figure 7. The streamlines wind tighter during the thrust rampup and peak thrust phases and get larger during the ramp down and minimum trust phases. The streamline patterns at the trailing edge, however, show stark differences from the cycle-averaged mean patterns. The streamlines during the rampup phase are open at the tailing edge of the rotor. They start closing at the peak of the cycle and get tighter as the cycle progresses toward its minimum, where the overall flow pattern becomes reminiscent of a VRS state in vertical descent. In line with the behavior of the streamlines, the vorticity remains compact at the leading edge, and is spread at the trailing edge. During the rampup phase the leading edge distribution is the most compact and the trailing edge most diffuse with a clear shear layer is present. None of the four phase in the figure similar ti the average flows in shown in figure 7.

Figure 9 shows the flow statistics of the combined flow shown in figure 7a over three thrust cycles which span over 118 rotor revolutions or 354 PIV planes. The figure presents vorticity and enstrophy, their centroids and their dispersion radii as captured by the composite flow field in figure 7 which is 4.63R×2.34R.

Total circulation history $\Gamma(t)$ qualitatively follows the thrust history. It, however, shows sign reversal, perhaps due to the limitation that the whole flow field was not captured. Therefore, a monotonic scaling of $C_T(t)$ and $\Gamma(t)$ is not possible. The mean circulation $< \Gamma >$ is finite (650 cm^2/s), several times that of an individual vortex filament (140 cm^2/s). Again this is due to finite wake view. The reversal the sign of the circulation $\Gamma(t)$ renders the centroid useless and dispersion radii calculations of equations 2 and 5. When $\Gamma(t)$ is at high values, vorticity centroid and dispersion radius are on the order of the disk radius R.

The enstrophy history $EN(t)$ shows sharp peaks that couple with the thrust cycle, the amplitude of which is almost twice the mean value. These peaks in figure 9 seems to be almost a superposition of those in figures 5 and 6. Since enstrophy EN is positive, its centroid and dispersion radius are well defined. Its centroid moves in phase with the thrust cycle, a weak coupling though. It is about 0.5R below and the lee side of the disk (cf. figure 7b). It does not move away substantially from its mean position. The spread of vorticity as measured by the enstrophy dispersion radius shows a strong coupling with the thrust. Vorticity is spread the widest at the trough of the thrust cycle and most compact at the crest as may be seen in the flow phase plotted (both streamline patterns and vorticity distributions) in figure 8 which is also confirmed in the vorticity movies of the composite flow field.

Conclusions

Time-resolved PIV experiments have been performed to investigate the Vortex Ring State of a rotor descending into its own wake. There are clear differences in the flow behavior over the leading and trailing edges of the rotor disk are observed. The flow field as marked by vorticity distribution highlights the changes in the flow topology. In particular, the contrast in the flow behavior at the leading and at the trailing edges are elucidated. The flow over the trailing edge exhibits large variations, whereas over the leading edge remains compact. Circulation and enstrophy histories at the trailing edge correlate wall with the thrust history of the rotor. The relationship between the thrust oscillation and the accumulation of vorticity around the rotor disk is less clear, but the trailing edge of the disk appears to drive the thrust oscillations as its modification of the flow field there is radical, ranging from a closed torus to an open vortex layer. It is likely that the center of thrust is off axis and oscillates in phase with the rest of the flow features. A limited number of VRS runs made with only one blade on the rotor corroborates the discussions and conclusions presented here.

Supported by NASA Ames Research Center Grant NCC2-5507.

References

[Betzina, 2001] Betzina, M. (2001). Tiltrotor descent aerodynamics: a small scale experimental investigation of vortex ring state. *57th American Helicopter Society Forum, Washington, D.C., USA, 9th-11th May.*

[Bhagwat and Leishman, 2000] Bhagwat, M. and Leishman, J. (2000). On the aerodynamic stability of helicopter rotor wakes. *56th AHS' Annual Forum, Virginia Beach, VA, USA, 2nd-4th May.*

[Brinson and Ellenrieder, 1998] Brinson, P. and Ellenrieder, T. (1998). Experimental investigation of the vortex ring condition. *24th European Rotorcraft Forum, Marseille, France, paper TE13.*

[Brown et al., 2004] Brown, R., Line, A., and Ahlin, G. (2004). Fuselage and tail-rotor interference effects on helicopter wake development in descending flight. *60th Annual Forum of the American Helicopter Society, Baltimore, MD, USA, 7th-10th June.*

[Cuerva et al., 2006] Cuerva, A., Sanz-Andres, A., Meseguer, J., and Espino, J. (2006). An engineering modification of the blade element momentum equation for vertical descent: fundamentals and validation. *Journal of the American Helicopter Society*, 51(4):341–348.

[Drees and Hendal, 1951] Drees, J. and Hendal, W. (1951). Airflow patterns in the neighbourhood of helicopter rotors. *Journal of Aircraft Engineering*, 23(266):107–111.

[Glauert, 1926] Glauert, H. (1926). The analysis of experimental results in the windmill brake and vortex ring state of an airscrew. *Aeronautical Research Committee, R&M 1026.*

[Green et al., 2005] Green, R., Gillies, E., and Brown, R. (2005). The flow field around a rotor in axial descent. *Journal of Fluid Mechanics*, 534:237–261.

[Green et al., 2007] Green, R., Savaş, Ö. and Caradonna, F. (2007). Visualisation and measurement of the vortex ring state of a descending rotor flow using time-resolved PIV. *PIV2007, Rome, Italy.*

[Johnson, 2004] Johnson, W. (2004). Model for vortex ring state influence on rotorcraft flight dynamics. *4th American Helicopter Society Decennial Specialists' Conference on Aeromechanics, San Francisco, CA, USA, 21st-23rd January.*

[Leishman, 2000] Leishman, J. (2000). *Principles of helicopter aerodynamics, 1st Edition.* Cambridge University Press, Cambridge, United Kingdom.

[Lock et al., 1925] Lock, C., Bateman, H., and Townend, H. (1925). An extension of the vortex theory of airscrews with applications to airscrews of small pitch, including experimental results,". *Aeronautical Research Committee, R&M 1014.*

[Newman et al., 2003] Newman, S., Brown, R., Perry, J., Lewis, S., Orchard, M., and Modha, A. (2003). Comparative numerical and experimental investigations of the vortex ring phenomenon in rotorcraft. *Journal of the American Helicopter Society*, 48(1):28–38.

[Spalart, 2003] Spalart, P. (2003). On the simple actuator disk. *Journal of Fluid Mechanics*, 494:399–405.

[Stack et al., 2005] Stack, J., Caradonna, F., and Savaş, Ö. (2005). Flow visualizations and extended thrust time histories of rotor vortex wakes in descent. *Journal of the American Helicopter Society*, 50(3):279–288.

[Stewart, 1951] Stewart, W. (1951). Helicopter behaviour in vortex ring conditions. *Aeronautics Research Council, R&M 2735.*

[Washizu et al., 1966] Washizu, K., Azuma, A., Koo, J., and Oka, T. (1966). Experiments on a model helicopter rotor operating in the vortex ring state. *Journal of Aircraft*, 3(3):225–230.

[Yaggy and Mort, 1963] Yaggy, P. and Mort, K. (1963). Wind-tunnel tests of two vtol propellers in descent. *NASA TN D-1766.*

[Batchelor (1967)] Batchelor, G. K. 1967 *An Introduction to Fluid Dynamics.* Cambridge University Press.

[Lamb (1938)] Lamb, H. 1938 *Hydrodynamics.* Dover.

[Ortega et al., 2003] Ortega, J. M., Bristol, R. L., and Savaş, Ö. (2003). Experimental study of the instability of unequal-strength counter-rotating vortex pairs. *Journal of Fluid Mechanics*, 474:35–84.

Figure 1: Rotor (radius $R = 12.7$ cm) and blade (chord $c = 1.9$ cm).

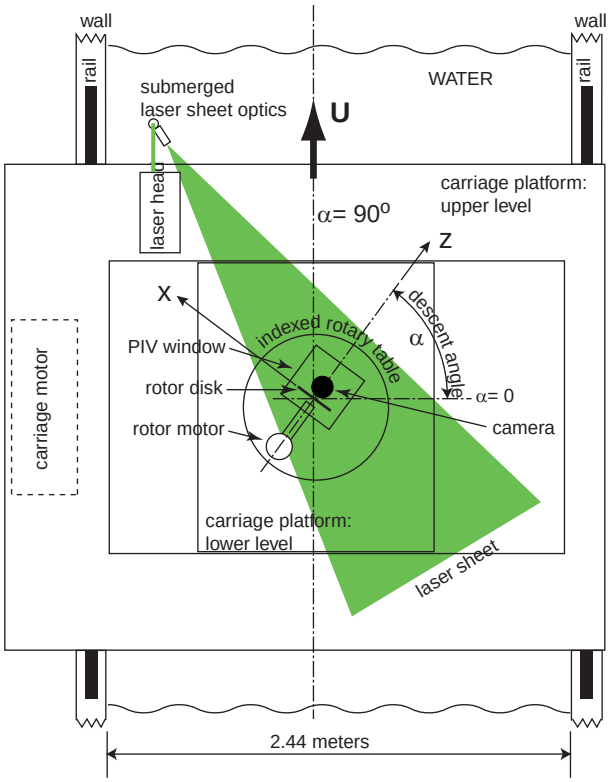

Figure 2: Plan view of the experimental setup. An xz-coordinate system is also defined. The descent velocity is $V_z = U sin\alpha$.

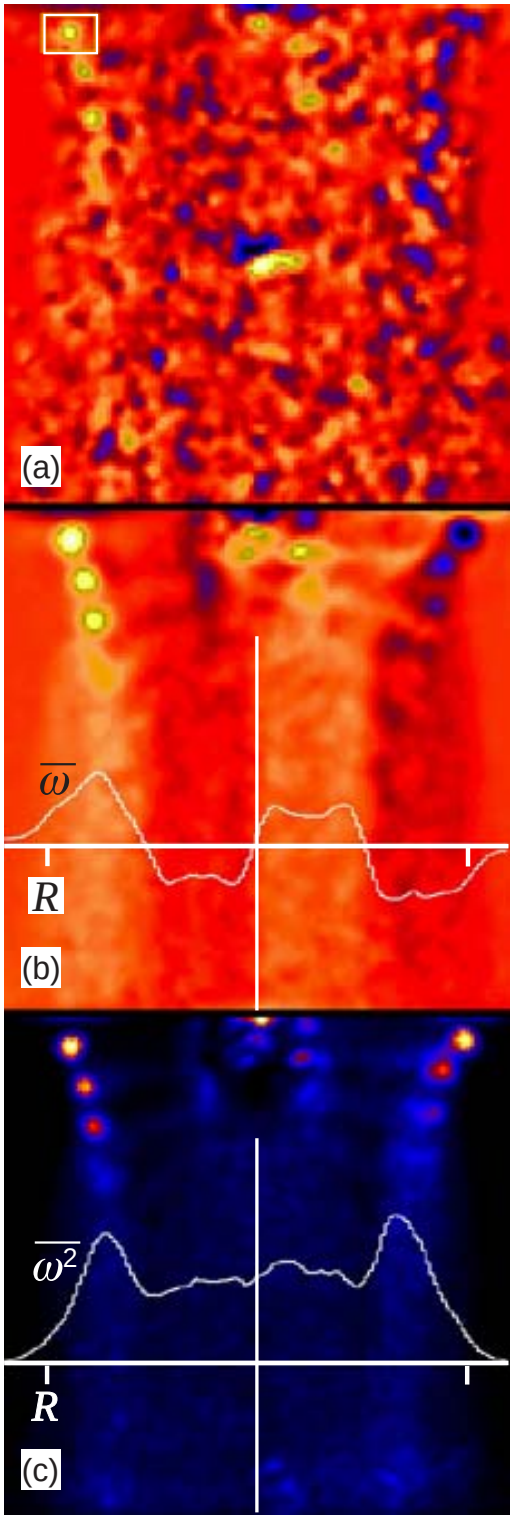

Figure 3: Vorticity field during hover (Flow 26: $n = 4\ Hz$, $C_T = 0.0092$, $V_h = 21.6$ cm/s). (a) instantaneous vorticity ω (PIV frame no 66), (b) average vorticity $< \omega >$ and (c) average enstrophy $< \omega^2 >$. Color scales: (a, b) yellow/white(+), blue/black(-), (c) black(0), yellow/white(+). The rectangular area at the upper right corner in (a) is used to estimate the vortex filament strength Γ_f.

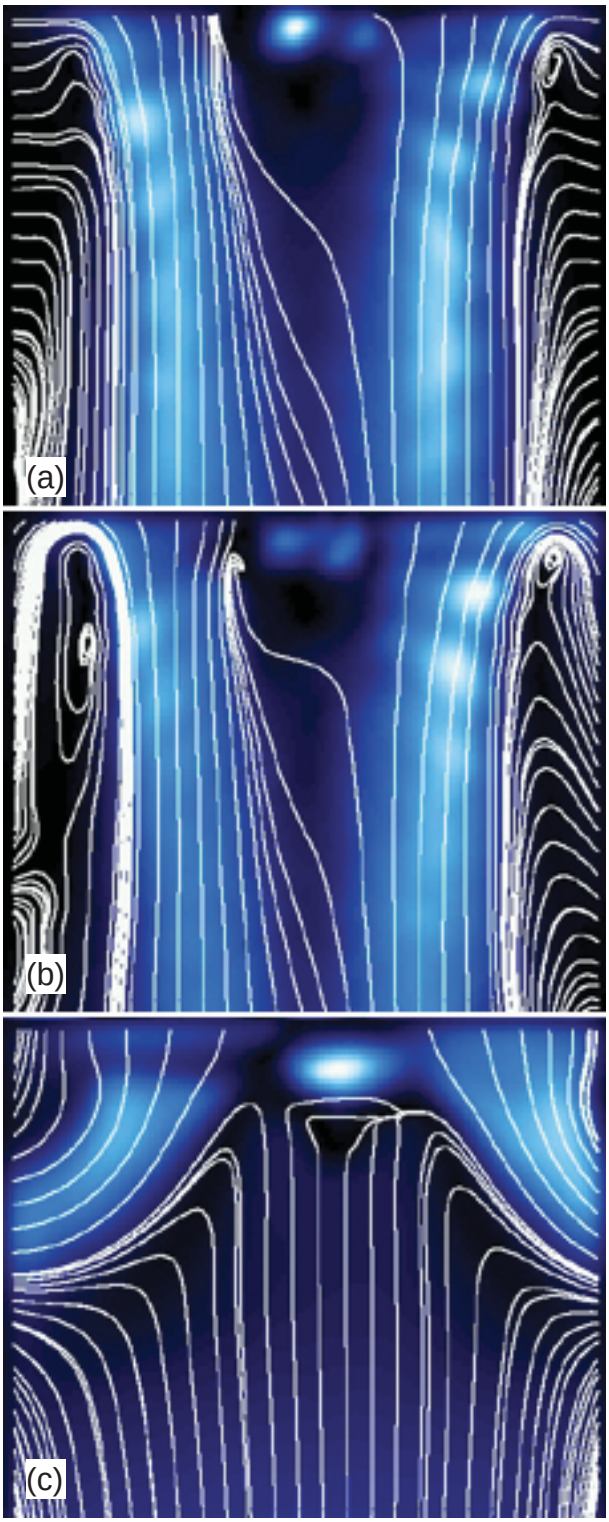

Figure 4: Mean streamline patterns, the backgrounds represent speed field, essentially displaying velocity fields. (a) hover (Flow 26: C_T=0.0092), (b) low speed descent (Flow 12: V_z=10 cm/s, C_T=0.0089, V_z/V_h=0.47, no shift), and (c) VRS in descent (Flow 161: V_z=25 cm/s, C_T=0.009, V_z/V_h=1.16, no shift).

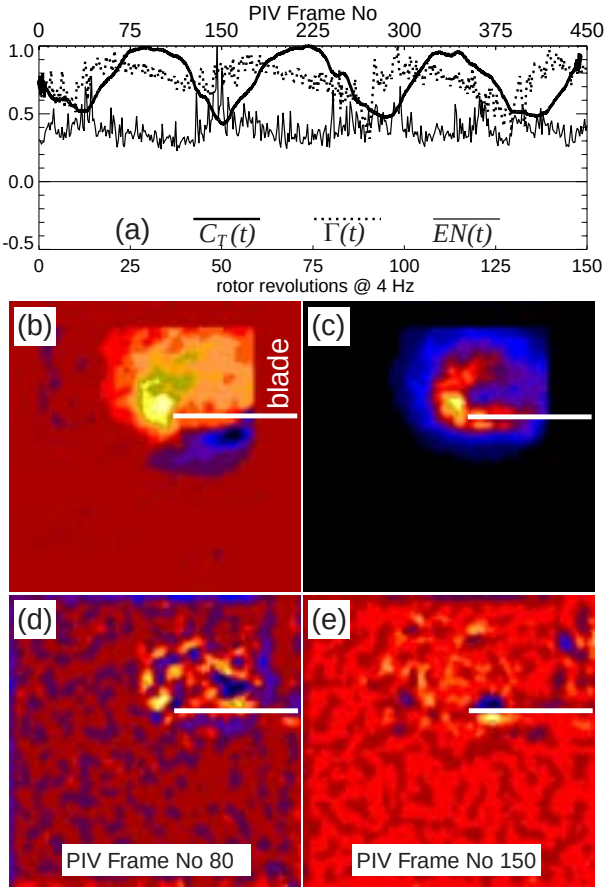

Figure 5: Leading edge dynamics at VRS. (figure 7, left: Flow 78: $n = 4\ Hz$, $\alpha = +60°$, $U = 25\ cm/s$, $C_\mathrm{T} = 0.011$) (a) Thrust, circulation, and enstrophy histories during VRS. (b) average vorticity field, (c) average enstrophy field, (d) vorticity field at peak thrust, and (e) vorticity field at minimum thrust during a VRS oscillation cycle. Color scales: (b, d, e) yellow/white(+), blue/black(-), (c) black(0), yellow/white(+).

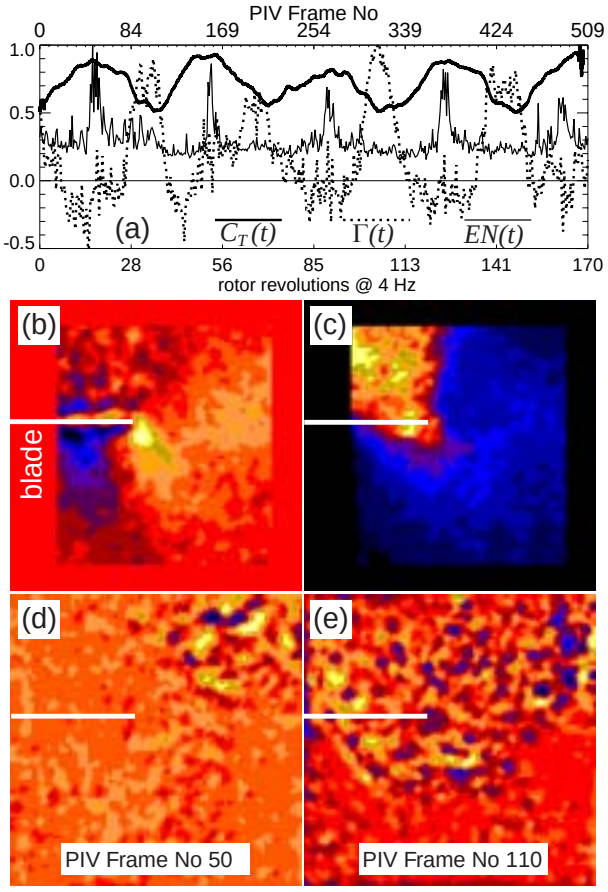

Figure 6: Trailing edge dynamics at VRS. (figure 7, right: Flow 94: $n = 4\ Hz$, $\alpha = -60°$, $U = 25\ cm/s$, $C_\mathrm{T} = 0.011$) (a) Thrust, circulation, and enstrophy histories during VRS. (b) average vorticity field, (c) average enstrophy field, (d) vorticity field at peak thrust, and (e) vorticity field at minimum thrust during a VRS oscillation cycle. Color scales: (b, d, e) yellow/white(+), blue/black(-), (c) black(0), yellow/white(+).

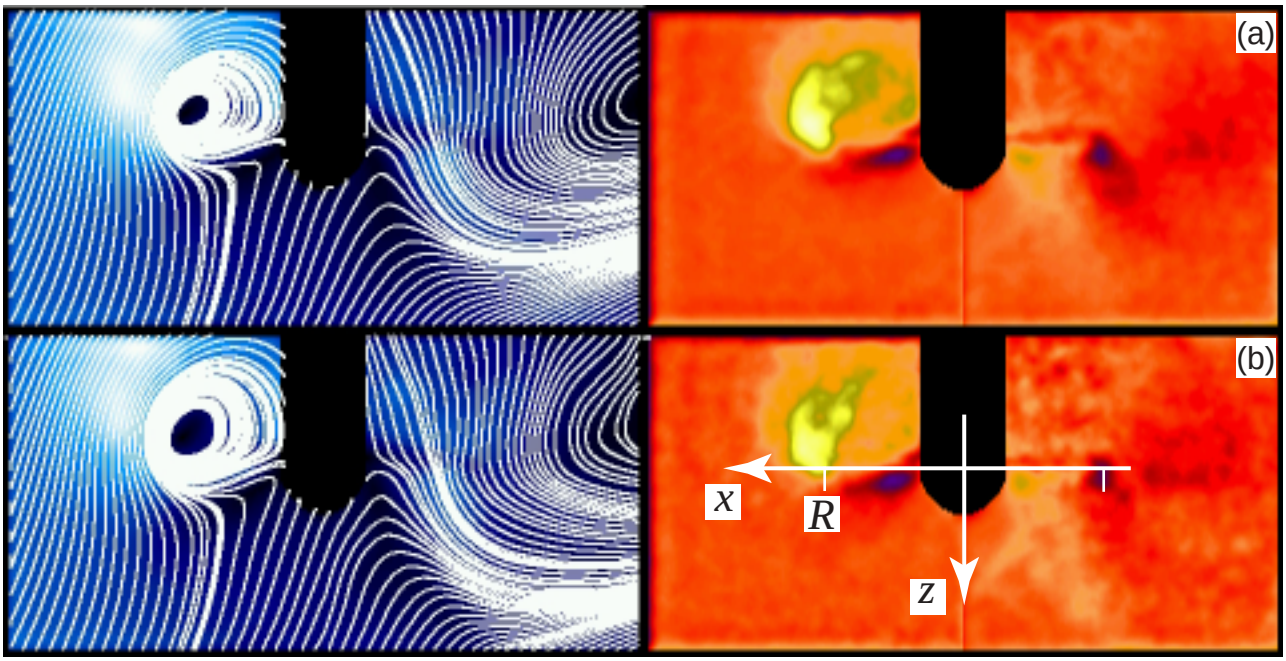

Figure 7: Averaged streamline (left) and vorticity (right) fields during VRS (Flows 78 & 94 shown in figures 5 & 6 are combined). The background color scale in the streamline plots indicates the average speed field, hence the total figure is a surrogate for the velocity vector field. The reconstructed view measures 58.8 cm $\times$ 29.9 cm (4.63R$\times$2.34R). (a) averaged over three thrust cycles ($40 \times 3 = 120$ revolutions) and (b) averaged over one thrust cycle (40 revolutions). The xz-coordinate system is defined in (b), where the rotor is in the $z = 0$ plane and the z axis is coincident with the rotor axis.

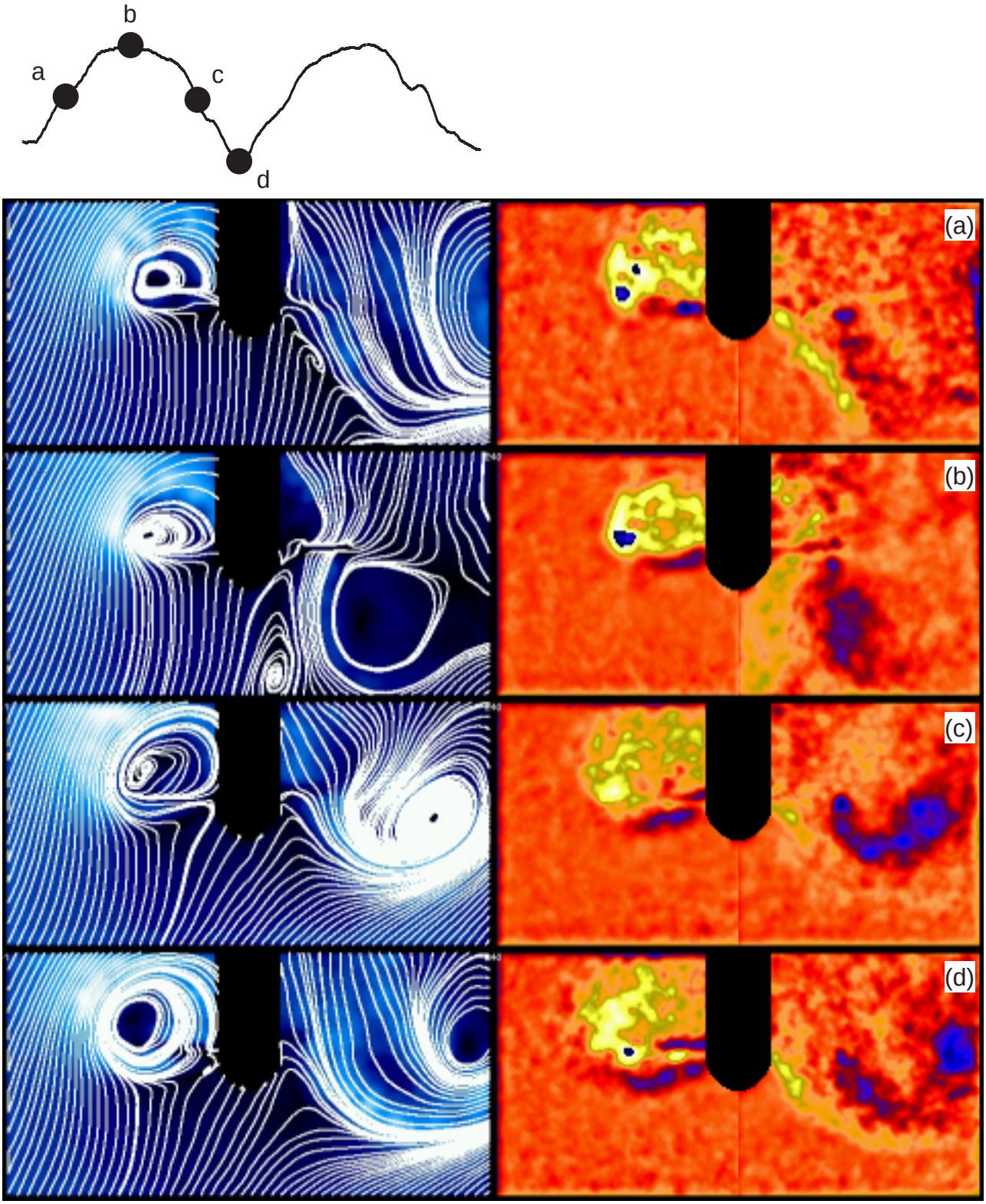

Figure 8: Flow fields at four salient points on the thrust cycle shown at the top (Flows 78 & 94 combined): (a) ramp up, (b) maximum thrust, (c) ramp down, and (d) minimum thrust. Streamlines over speed (left column) and vorticity (right column) are shown. Frames are constructed from local averages on the thrust cycle. The streamlines patterns have the same seed points. The same color scheme is used in the vorticity plots. Note that the color scale is folded over at positive vorticity in a, b, and d; marking the extreme positive values.

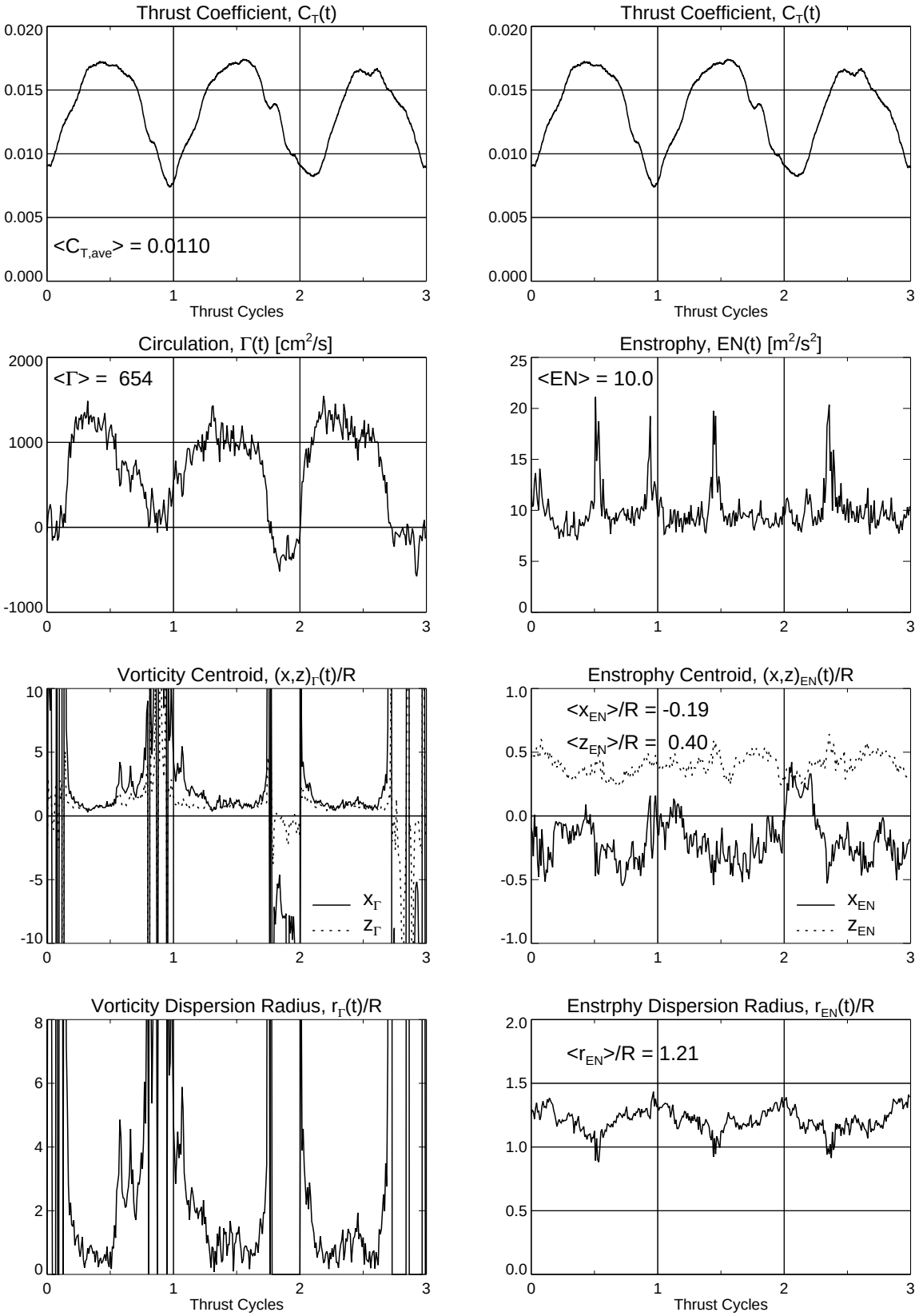

Figure 9: Vorticity (left) and enstrophy (right) statistics. Vorticity centroid and dispersion radius defined in equations 2 and 5 become undefined at $\Gamma(t)$ zero-crossings. One thrust cycle corresponds to about 40 rotor revolutions and $R = 12.7$ cm. The thrust history recorded during the leading edge measurements is plotted for reference. The xz-coordinate system is define in figures 2 and 7.